RESEARCH ARTICLE
Editor's Choice
ADVANCED MATERIALS
www.advmat.de

Novel Palladium Hydride Surface Enabling Simultaneous Bacterial Killing and Osteogenic Formation through Proton Capturing and Activation of Antioxidant System in Immune Microenvironments

Dongdong Zhang, Mei Li, Shuhan Chen, Huihui Du, Hua Zhong, Jun Wu, Feihong Liu, Qian Zhang, Feng Peng, Xuanyong Liu,* and Kelvin W.K. Yeung**

Achieving bacterial killing and osteogenic formation on an implant surface rarely occurs. In this study, a novel surface design–a palladium hydride (PdH_x) film that enables these two distinct features to coexist is introduced. The PdH_x lattice captures protons in the extracellular microenvironment of bacteria, disrupting their normal metabolic activities, such as ATP synthesis, nutrient co-transport, and oxidative stress. This disruption leads to significant bacterial death, as evidenced by RNA sequence analysis. Additionally, the unique enzymatic activity and hydrogen-loading properties of PdH_x activate the human antioxidant system, resulting in the rapid clearance of reactive oxygen species. This process reshapes the osteogenic immune microenvironment, promoting accelerated osteogenesis. These findings reveal that the downregulation of the NOD-like receptor signaling pathway is critical for activating immune cells toward M2 phenotype polarization. This novel surface design provides new strategies for modifying implant coatings to simultaneously prevent bacterial infection, reduce inflammation, and enhance tissue regeneration, making it a noteworthy contribution to the field of advanced materials.

1. Introduction

Orthopedic implants have the potential to significantly improve patients' quality of life by restoring mobility and function in damaged or missing bones.[1–3] With the global rise in orthopedic diseases due to aging populations and increased healthcare awareness, the demand for these implants continues to grow.[4] However, several challenges remain in ensuring the efficacy and accessibility of orthopedic implants for clinical therapy. Complications such as early bacterial infection, immune rejection, inflammatory response, and osseointegration loosening can lead to premature failure of implants, delayed union and nonunion, and local dysfunction or damage to bone tissue.[5–7] Consequently, researchers may consider to minimize the need for the

D. Zhang, J. Wu, F. Liu, Q. Zhang, K. W. Yeung
Shenzhen Key Laboratory for Innovative Technology in Orthopedic Trauma
Department of Orthopaedics and Traumatology
The University of Hong Kong-Shenzhen Hospital
Shenzhen 518053, China
E-mail: wkkyeung@hku.hk

M. Li, F. Peng
Medical Research Institute
Department of Orthopedics
Guangdong Provincial People's Hospital (Guangdong Academy of Medical Sciences)
Southern Medical University
Guangzhou 510080, China
E-mail: pengfeng@gdph.org.cn

The ORCID identification number(s) for the author(s) of this article can be found under https://doi.org/10.1002/adma.202404485

DOI: 10.1002/adma.202404485

S. Chen, H. Du, X. Liu
State Key Laboratory of High Performance Ceramics and Superfine Microstructure
Shanghai Institute of Ceramics
Chinese Academy of Sciences
Shanghai 200050, China
E-mail: xyliu@mail.sic.ac.cn

S. Chen, H. Du, X. Liu
Center of Materials Science and Optoelectronics Engineering
University of Chinese Academy of Sciences
Beijing 100049, China

H. Zhong
Department of Orthopaedics
The Fifth Affiliated Hospital
Southerm Medical University
Guangzhou 510009, China

J. Wu, Q. Zhang, K. W. Yeung
Department of Orthopaedics & Traumatology
School of Clinical Medicine, Li Ka Shing Faculty of Medicine
The University of Hong Kong
Pokfulam, Hong Kong 999077, China

removal of failed implants and subsequent medication and surgical interventions. Surface modifications of orthopedic implants, including special surface structures, drug/bioreagent-loading layers, and external light/ultrasonic-responsive films, have been explored as potential solutions to reduce implant failure.[8,9] However, these strategies have not been widely adopted due to inherent limitations such as inefficiency, antibiotic resistance, systemic toxicity, and complex preparation processes.[10,11] Considering the distinct microenvironments and biological mechanisms of bacteria, bone-related cells, and immune cells, this study aims to develop a biosafe surface that exhibits specific biomedical functions when interacting with particular bacteria or cells in their unique microenvironments.

Currently, antibacterial research focuses on drug/chemo-based, reactive oxygen species (ROS)-mediated, and field-heating sterilization methods, resulting in the development of various advanced biomaterials and designs.[12–16] However, these strategies are incapable of selectively killing bacterial cells while sparing normal mammalian cells. To address this issue, a new approach can be proposed by exploiting the metabolic differences between mammalian and bacterial cells. Respiration, a critical process for energy metabolism in living organisms, is essential for maintaining their normal function.[17,18] Notably, bacterial respiration occurs on the bacterial membrane, while mammalian respiration takes place on the mitochondrial membrane.[19] This metabolic distinction provides an opportunity for a novel treatment strategy that enables targeted bacterial killing without harming normal cells. Furthermore, proton transfer plays a role in the respiration and energy metabolism of living bacteria and cells.[20] A stable proton concentration gradient between the interior and exterior of the bacterial membrane is crucial for adenosine triphosphate (ATP) production, nutrient co-transport, and intracellular redox reactions.[21,22] Antimicrobial drugs can disrupt the energy metabolism of microorganisms by inhibiting proton pump function, leading to impaired cell function. Common proton pump inhibitors, such as omeprazole and lansoprazole, are primarily used to treat excessive stomach acid and gastric ulcers but also exhibit antimicrobial activity against specific microorganisms. Based on these findings, we propose that bacterial metabolism and cell fate can be differentiated by interfering with proton transfer.

Interestingly, palladium (Pd) atoms have been identified can readily bind to hydrogen atoms, allowing Pd nanocrystals to store proton (form PdH_x) and release H_2 through their lattices at room temperature.[23] To maintain the proton concentration gradient, bacteria need to transfer intracellular protons to the extracellular space. Therefore, we propose that the 5s electron layer of Pd atoms can be utilized to conjugate protons, drawing them into the PdH_x lattice and effectively consuming them in the microenvironment outside the bacterial membrane. This process can then disrupt bacterial respiration and ultimately lead to their death. Simultaneously, PdH_x nanostructures possess a variety of antioxidant enzymatic activities akin to natural enzymes.[23] Recent studies have demonstrated that due to its exceptional transmembrane capacity, hydrogen (H_2) can act as a Trojan horse, effectively infiltrating bacterial biofilms. Subsequently, H_2 considerably hampers bacterial metabolism by modulating adenosine triphosphate (ATP) and nicotinamide adenine dinucleotide (NADH).[24,25] Moreover, the released H_2 from PdH_x serves as an endogenous gas and an antioxidant with essential physiological and pathological regulatory functions, demonstrating significant therapeutic effects on various diseases, such as atherosclerosis, Alzheimer's disease, arthritis, dermatitis, colitis, hepatitis, and pancreatitis.[26,27] Indeed, the human body's antioxidant defense system consists of antioxidant enzymes and antioxidants, which play crucial biological roles in regulating macrophages, wound repair, and preventing nerve damage.[28] Biomimetic nanoenzymes hold the potential in regulating the bone immune microenvironment, achieving anti-inflammatory effects, and promoting osteogenesis and angiogenesis.[10] Hence, we believe that the unique enzymatic activity and hydrogen-loading characteristics of PdH_x can effectively function as a biomaterial-based antioxidant system, leading to rapid clearance of ROS and promoting the conversion of macrophages to the anti-inflammatory M2 type.[29]

In this study, we hypothesized that PdH_x film-modified metallic implants can exhibit dual bactericidal and osteogenic immune microenvironment regulatory functions through the mechanism of "capture and release" of protons (**Scheme 1**). The PdH_x film-modified titanium (Ti) implant can be tailor-made by employing ion sputtering and immersion treatment under H_2 gas flow at room temperature. We investigated the material characterizations and physicochemical properties, such as film characteristics, hydrogen release behavior, and enzyme-like activity. Additionally, we examined the biological effects of the PdH_x films on bacteria, macrophages, and bone-related cells using transcriptome sequencing and intracellular molecular assays. Moreover, we evaluated the in vivo treatment effect on various conditions, including subcutaneous air sac, normal bone defect, and infected bone defect.

2. Results and Discussion

2.1. Characterization and Physicochemical Properties

Figure 1 shows a schematic overview of the film's preparation and its fundamental characterizations. The PdH_x film was prepared on a Ti substrate using a novel two-step method (Figure 1a). The substrate was coated with Pd using ion sputtering, and H_2 was loaded onto the film by immersing the sample in H_2 gas flow at room temperature. Pd nanocrystals are excellent chemical hydrogen storage materials, and hydrogen molecules move to the surface of Pd under normal temperatures.[30,31] During Pd-mediated catalysis, the hydrogen molecule splits into two hydrogen atoms and forms an unstable chemical bond with the Pd atoms. The hydrogen atoms are stored in the Pd lattice to form PdH_x (reaction 1), which is a reversible process. Subsequently, the hydrogen atoms can slowly break away from the Pd lattice, reforming into hydrogen molecules (reaction 2).

$$Pd + xH^+ \rightarrow PdH_x \quad (1)$$

X. Liu
School of Chemistry and Materials Science
Hangzhou Institute for Advanced Study
University of Chinese Academy of Sciences
1 Sub-lane Xiangshan, Hangzhou 310024, China

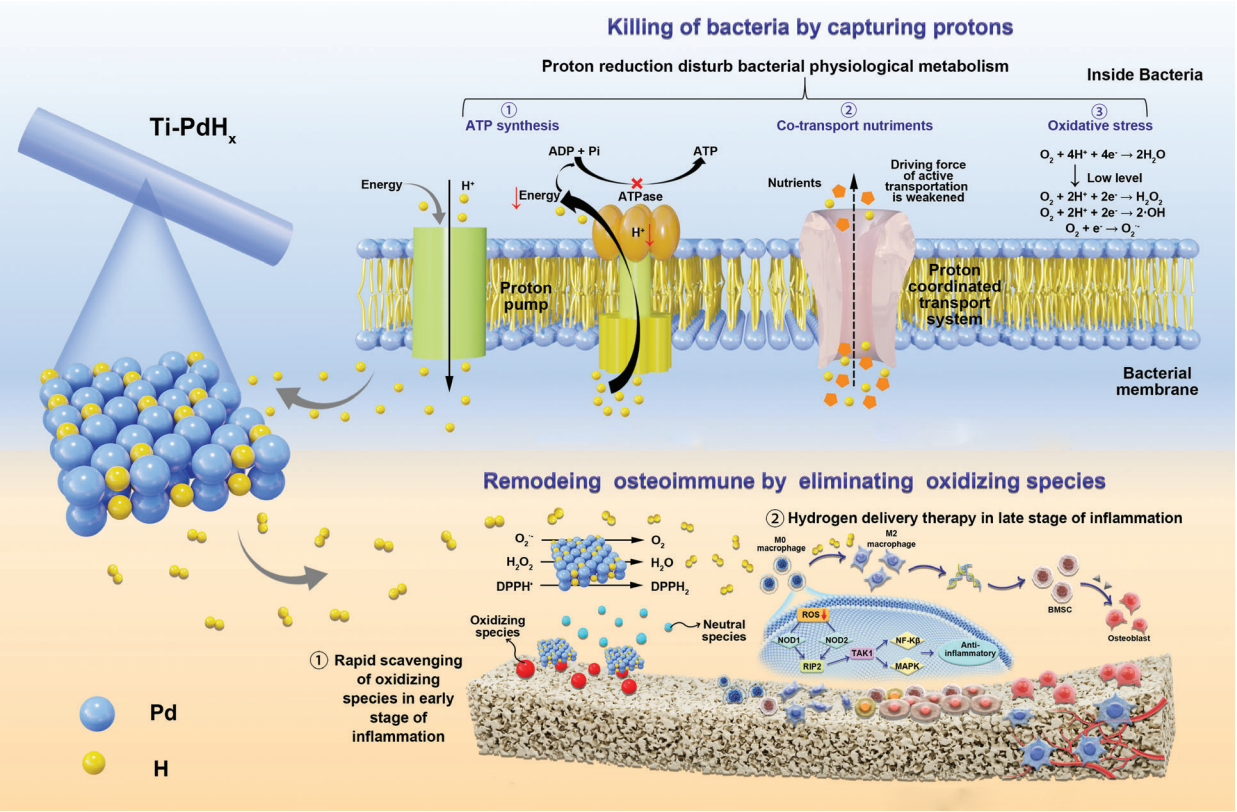

Scheme 1. Schematic illustration of the mechanism of the proton transfer-mediated bacterial killing with the enzymic osteogenic immune microenvironment remodeling on titanium implants.

$$PdH_x \rightarrow Pd + (1x)/2H_2 \quad (2)$$

The pristine Ti surface exhibits a flat and smooth morphology (Figure 1b), which, after Pd deposition, transitioned to a nanoscale roughness (Figure 1c). Following H_2 loading, the insertion of protons into the Pd lattice induced film expansion and subsequent microcracking (Figure 1d). The film's thinness precluded the X-ray diffraction (XRD) analysis from revealing characteristic peaks (Figure S1, Supporting Information). Transmission electron microscopy (TEM) provided further insights, with sample preparations being made using focused ion beam milling to afford a cross-sectional view of the PdH_x film (Figure 1e). Given the minimal size of hydrogen atoms and their location within the Pd lattice's interstitial gaps, the Pd atomic arrangement remains unaffected. Consequently, the TEM diffraction patterns confirmed this, exhibiting the (222) and (200) crystal plane structures. The PdH_x thin film maintained direct atomic contact with the Ti substrate, exhibiting no discernible voids and secure bonding. The film's thickness was measured at ≈50 nm (Figure 1f). Only elements Pd, Ti, and O were detected in the X-ray photoelectron spectroscopy (XPS) spectra (Figure 1g). The Pd film, initially dark blue, transitioned in hue to light brown upon H_2 absorption, reflecting the materials' changing surface characteristics (Figure 1h). The observed increase in surface contact angle is attributable to the hydrophobic characteristics of the gas molecules. Furthermore, a reduction in corrosion current density suggests that both Ti-Pd and Ti-PdH_x exhibit improved corrosion resistance compared to the untreated Ti substrate, as detailed in Figure S2 (Supporting Information).

To assess the hydrogen release behavior of Ti-PdH_x, 2,2-diphenyl-1-picrylhydrazyl (DPPH•) was chosen as the oxidative probe. DPPH• is stable, exhibiting a purple color without a catalyst throughout the testing duration. A color fade signifies the reduction of DPPH•, with the emitted reductive hydrogen quantifiable by the absorption peak decrease at 517 nm. **Figure 2a** depicts a pronounced hydrogen release within the first 3 h, attributed to the significant hydrogen adsorption on the Ti-PdH_x surface. Approximately 45% of hydrogen was released from Ti-PdH_x after 33 h. The film's peroxidase-like activity was gauged using a 3,3′,5,5′-tetramethylbenzidine (TMB) assay, indicating that both Pd and PdH_x films do not generate ROS at 37 °C in saline solution (Figure 2b). Additionally, the antioxidant enzyme-mimicking and free radical-scavenging capacities of PdH_x film were examined (Figure 2c), with the introduction of H_2 potentially enhancing Ti-PdH_x's antioxidant characteristics. The superoxide radical ($O_2^{\bullet-}$) scavenging represents the initial phase of the antioxidant cascade. Ti, Ti-Pd, and Ti-PdH_x's superoxide dismutase (SOD)-like activities underwent assessment via a WST-8 colorimetric assay, with the absorption spectra and quantitative outcomes presented in Figure 2d,g, respectively. The suppression efficacy on $O_2^{\bullet-}$ for Ti, Ti-Pd, and Ti-PdH_x is less than 10%, and progresses in the order of Ti < Ti-Pd < Ti-PdHx. The subsequent cascade stage involves the removal of H_2O_2 generated by SOD catalysis. The catalase (CAT)-like intrinsic activities of

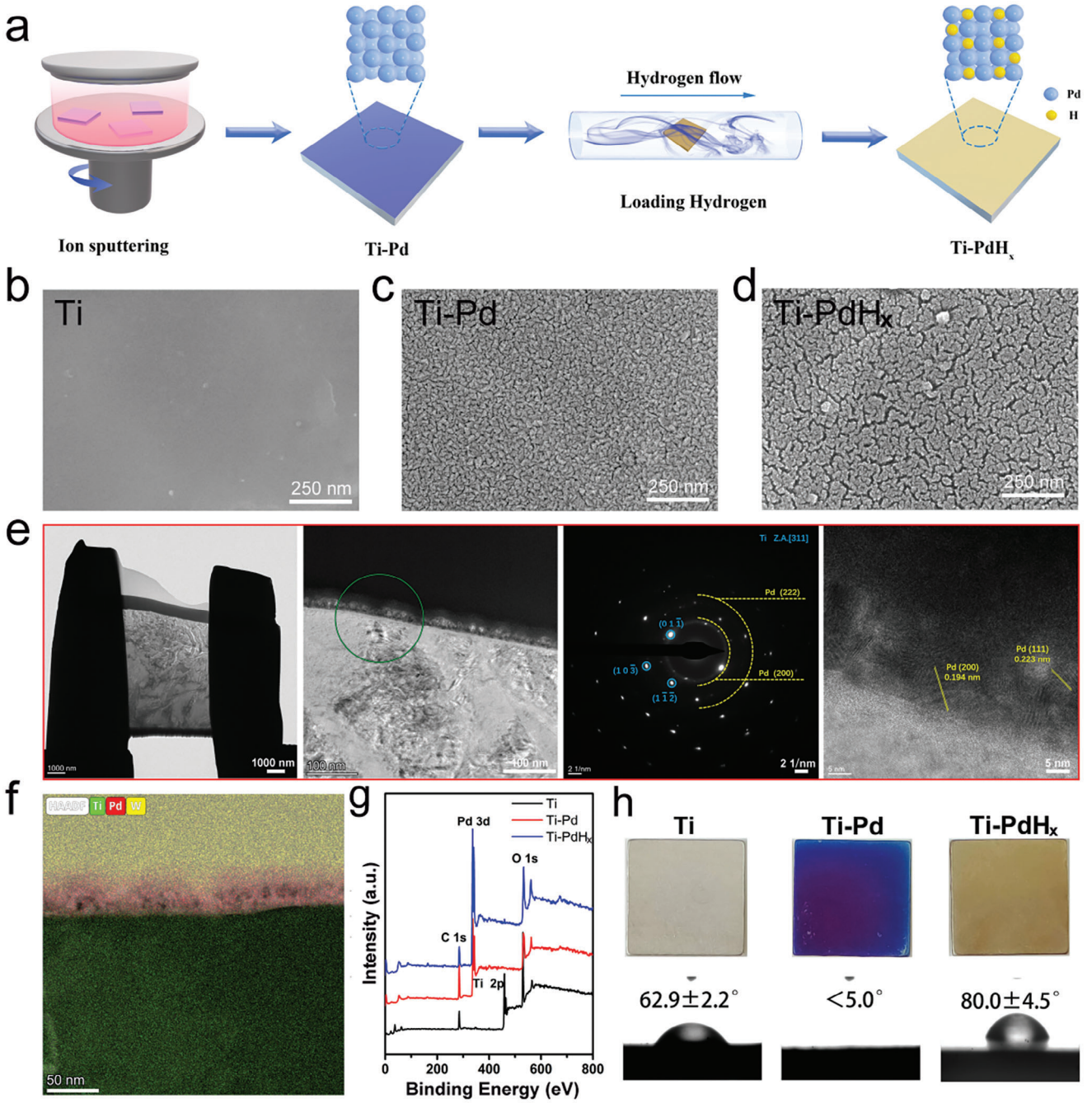

Figure 1. Schematic illustration of the preparation process of Ti-Pd and Ti-PdH$_x$ samples (a). Surface scanning electron microscopy morphologies of Ti, Ti-Pd, and Ti-PdH$_x$ (b–d). Transmission electron microscopy images (e) and the energy-dispersive X-ray spectroscopy spectrum (f) of PdH$_x$ film. X-ray photoelectron spectroscopy spectra (g), digital photos, and water contact angle (h) of Ti, Ti-Pd, and Ti-PdH$_x$.

Ti, Ti-Pd, and Ti-PdH$_x$ were analyzed by monitoring the breakdown of 10 mM H_2O_2 into water and oxygen. The diminishing absorbance at 405 nm evident in Figure 2e signals H_2O_2 consumption within the reaction. Ti-PdH$_x$ demonstrated the swiftest H_2O_2 elimination (Figure 2h), reaching a 94.6% scavenging rate within 12 h and displaying superior catalytic prowess relative to Ti (−0.4%) and Ti-Pd (83.3%). The remarkable CAT-like and SOD-like functions of the PdHx films are ascribed to the prominently exposed Pd (111) crystal facet, which, as reported, possesses greater antioxidant capabilities than Pd (100) facets, due to reduced surface energies.[32] The comprehensive antioxidant capacities of Ti, Ti-Pd, and Ti-PdH$_x$ were appraised with a DPPH• colorimetric assay at an absorption of 517 nm. Given atomic hydrogen's potent reductive power, Ti-PdH$_x$ exhibited a significant leap in total antioxidant capacity after hydrogen loading, soaring from 10.4% to 64.4% (Figure 2f,i).

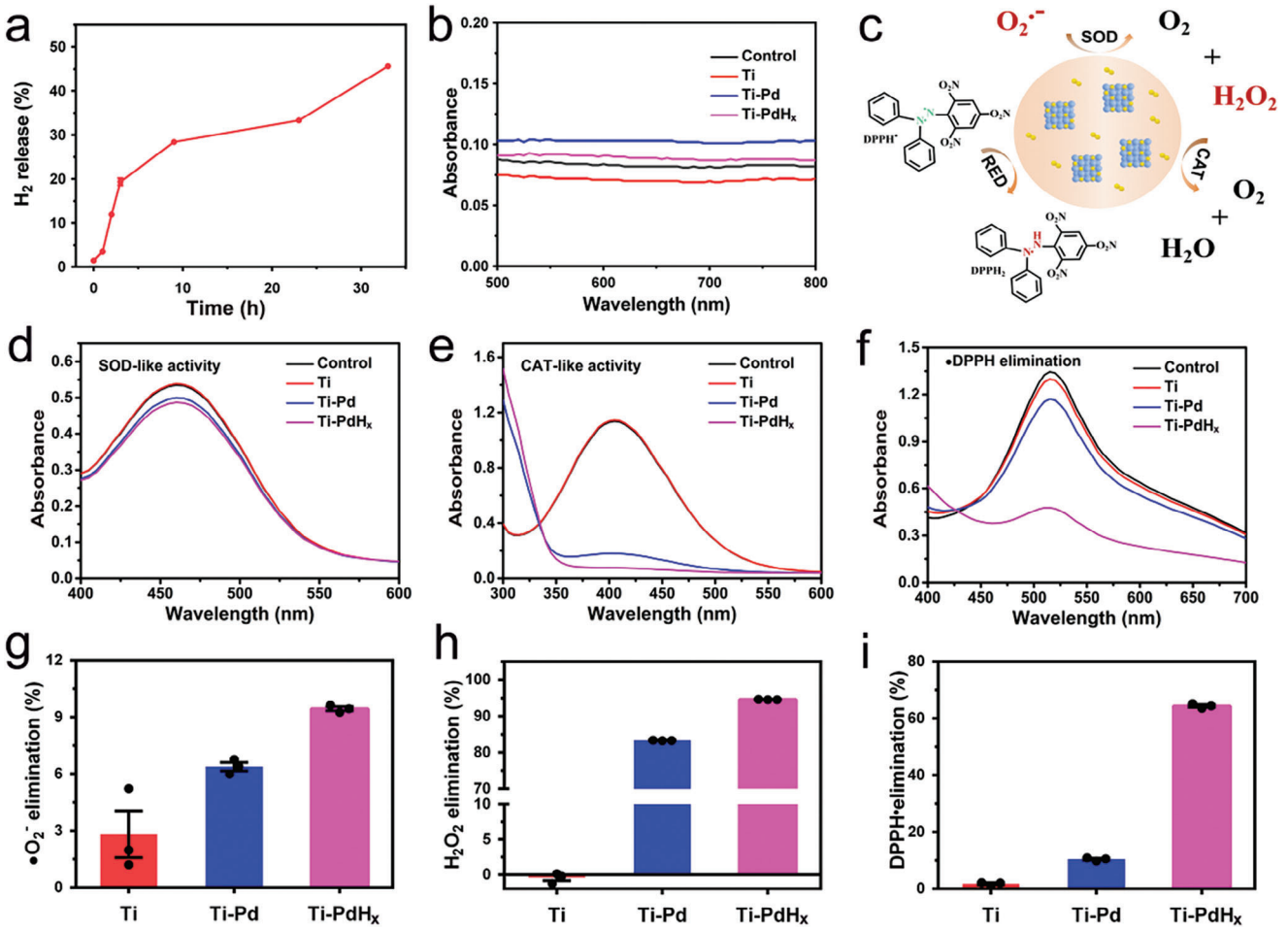

Figure 2. Hydrogen release behavior of Ti-PdH$_x$ in PBS solution at 37 °C (a). UV–vis spectra of TMB to determine the production of reactive oxygen species under simulated bacterial culture conditions for Ti, Ti-Pd, and Ti-PdH$_x$ (b). Schematic illustration of the enzyme catalytic activity of Ti-PdH$_x$ (c). UV–vis spectra of WST-B and corresponding quantitative results to determine the SOD-like (d,g), CAT-like (e,h), and DPPH• scavenging (f,i) activity of Ti, Ti-Pd, and Ti-PdH$_x$.

2.2. Antibacterial Performance and Mechanism Verification

Staphylococcus aureus (*S. aureus*), a gram-positive bacterium known for its propensity to infect orthopedic trauma and implants, was selected to assess the antibacterial activity of the samples.[33] **Figure** 3a indicates that Ti-Pd and Ti-PdH$_x$ samples supported the growth of fewer bacterial colonies compared to the Ti samples, signifying enhanced antibacterial properties. This finding was corroborated by tests conducted with *Escherichia coli* (*E. coli*), as illustrated in Figure S3 (Supporting Information). Live/dead bacterial stain analyses showed intense green fluorescence, indicative of a preponderance of viable bacteria on the Ti surfaces, whereas Ti-Pd and Ti-PdH$_x$ exhibited markedly fewer live bacteria (Figure 3b). Cell viability assessments of *S. aureus* substantiated this observation, with the highest survival on Ti, followed by Ti-PdH$_x$ and Ti-Pd, in descending order (Figure 3c). This trend was mirrored in ATP synthesis levels among the samples, as depicted in Figure 3d. Furthermore, 5-cyano-2,3-ditolyl Tetrazolium Chloride (CTC) indicated that bacterial respiration was notably diminished on Ti-Pd and Ti-PdH$_x$ compared to untreated Ti (Figure 3e). ROS fluorescence staining suggested that both Ti-Pd and Ti-PdH$_x$ elicited intrabacterial ROS production, signifying oxidative stress in the bacteria (Figure 3f). It is critical to note that although enzymatic assays indicated that Pd and PdH$_x$ films did not generate ROS in physiological saline at 37 °C but scavenged them instead (Figure 2). In addition, minor variations in contact angle are anticipated to exert a negligible influence on the antibacterial efficacy. Since the magnitude of the contact angle predominantly reflects the water contact angle of a surface under ambient air conditions. Nonetheless, when a surface is subjected to prolonged exposure to a liquid environment, it is expected to achieve a state of complete wetting eventually. Therefore, these films must possess unique antibacterial mechanisms that prompt extensive metabolic disturbances in bacteria. Remarkably, Ti-PdH$_x$ demonstrated marginally reduced antibacterial efficacy compared to Ti-Pd. Pursuing this observation, Ti-Pd was subjected to a 24-hour hydrogen gas flow (denoted as Ti-PdH) to increase proton loading beyond that of Ti-PdH$_x$. The resulting antibacterial activity hierarchy against *S. aureus* was Ti-Pd > Ti-PdH$_x$ > Ti-PdH (Figure S4, Supporting Information), suggesting a direct correlation between stored proton levels in the Pd lattice and diminished antibacterial potency.

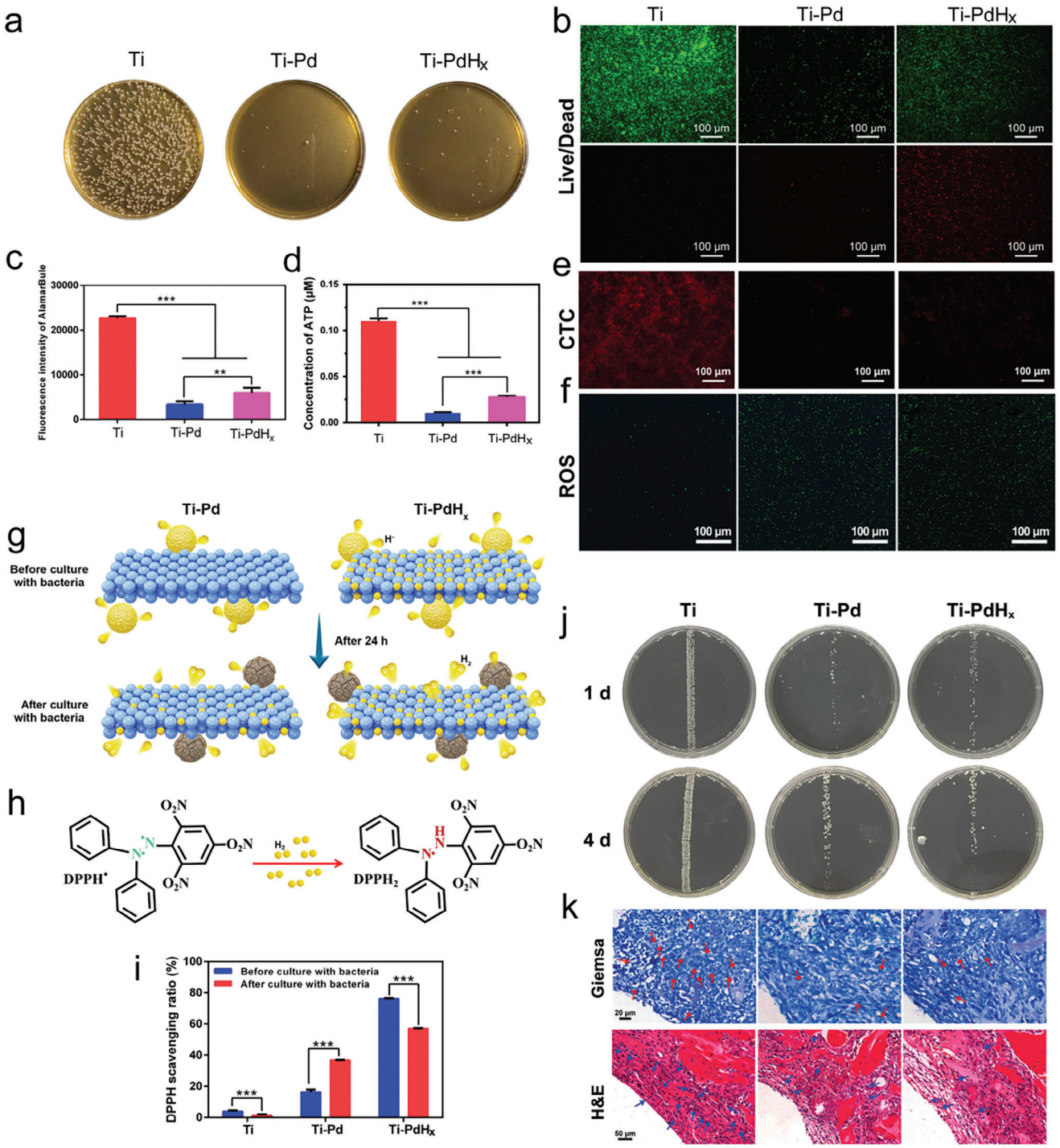

Figure 3. Antibacterial performance evaluation of Ti, Ti-Pd, and Ti-PdH_x. In vitro tests: representative culture images of bacterial colonies (a); live/dead staining (b); cell activity (c); ATP level (d); CTC staining (e); ROS staining (f); schematic diagram of PdH_x film capturing bacterial protons before and after bacterial coculture (g); schematic diagram of hydrogen reduction of DPPH• to $DPPH_2$ (h); DPPH• scavenging activity before and after bacterial coculture (i). In vivo tests: representative culture images of bacterial colonies for 1 and 4 days (j); Giemsa and hematoxylin & eosin staining. Extensive lymphocyte and neutrophil infiltration are shown with red arrows; bacteria are shown with blue arrows (k).

As a natural and excellent hydrogen storage material, Pd binds with hydrogen atoms, maybe thereby interfering with the proton transport process in bacteria and leading to their death. To investigate the proton transfer from *S. aureus* to the Ti-Pd and Ti-PdH_x surfaces, a specialized experiment was conducted, delineated in the schematic of Figure 3g. The oxidative probe DPPH• serves as a detector of sample reducibility, indicating their hydrogen retention and release capabilities (Figure 3h). Generally, the greater the quantity of protons retained in the Pd lattice, the more potent the sample's ability to neutralize DPPH• (Figure S5, Supporting Information). We evaluated the DPPH• scavenging activities of Ti, Ti-Pd, and Ti-PdH_x both before and after exposure to bacterial cultures, with the findings presented in Figure 3i. Ti served as a baseline, demonstrating unchanged reducibility subsequent to bacterial culturing. In marked contrast, Ti-Pd's scavenging effectiveness improved post-culture, attributable to the Pd coating's capacity to store protons and emit reductive hydrogen. This pronounced alteration suggests that the Pd overlay seizes extracellular bacterial protons, incorporating them into its lattice for subsequent storage while engaging in bacterial cultivation. Conversely, for the Ti-PdH_x variant, the DPPH• scavenging proficiency diminished post-culture, a consequence of the hydrogen expelled surpassing that which was initially conserved during the bacterial incubation. Pd and PdH_x kill bacteria by capturing the bacterial protons. This antibacterial mechanism determines that their antibacterial performance is related to the inherent proton content in the lattice; the higher the proton content, the weaker the antibacterial ability.

The in vivo antibacterial activity of the samples was also investigated using a mouse model implanted with *S. aureus*-infected biofilm as a carrier. The in vivo results, as shown in Figure 3j,k, demonstrated that the raw Ti group exhibited substantial bacterial colony growth. By contrast, the Ti-Pd and Ti-PdH_x groups displayed fewer bacterial colonies, indicating that they effectively inhibited bacterial growth in vivo. Histopathological changes in the femurs of each group were observed using hematoxylin and eosin (H&E) staining, and the presence of residual bacteria was visualized using Giemsa staining. H&E staining revealed typical features of tissue infection in samples from the raw Ti groups, including extensive lymphocyte and neutrophil infiltration, where the bone tissues were in contact with the implants. Moreover, numerous bacteria were observed in the Ti groups by Giemsa staining. The Ti-Pd and Ti-PdH_x groups showed weaker inflammatory reactions, and the bacteria were reduced to almost invisible levels, illustrating their excellent antibacterial properties in vivo.

Transcriptome sequence analysis was performed to explore the antibacterial mechanisms of Ti-PdH_x. The total raw reads for Ti and Ti-PdH_x were 3.97 and 4.02 million, respectively, whereas the clean-read rates were 99.37% and 99.73%, respectively. The Pearson correlation values indicate good clustering between the Ti and Ti-PdH_x groups (Figure S6, Supporting Information). The samples showed a significant difference in the first principal component (Figure S7, Supporting Information), demonstrating that the Ti-PdH_x surface had a noticeable impact on *S. aureus* gene expression. **Figure** 4a shows a volcano plot of the differentially expressed genes (DEGs). There were 180 DEGs, of which 62 were upregulated and 118 were downregulated. To further analyze the exact functions of these genes, the Kyoto Encyclopedia of Genes and Genomes (KEGG) and Gene Ontology (GO) enrichment analyses were performed. As shown in Figure 4b, the top 20 pathways in the KEGG terms mainly focused on the biosynthesis and metabolism of various amino acids, including *D*-amino acids, histidine, arginine, proline, alanine, aspartate, glutamate, lysine, cysteine, methionine, valine, leucine, and isoleucine. For the top 20 enriched biological processes by GO (Figure 4c), 18 were downregulated, and 13 were related to amino acid metabolic and biosynthetic processes. Therefore, both the KEGG and GO enrichment analyses demonstrated that amino acid-related behaviors were suppressed by the PdH_x film. In terms of molecular function (Figure 4d), antioxidant, peroxidase, and oxidoreductase activities were all upregulated, suggesting that oxidative behaviors were enhanced, providing evidence that bacteria cultured on the Ti-PdH_x surface may encounter oxidative stress damage. Notably, compared with the Ti group, the bacteria cultured on the Ti-PdH_x surface exhibited lower nicotinamide adenine dinucleotide phosphate (NADP) and lyase (especially hydro-lyase and carbon-oxygen lyase) activities. NADP is a coenzyme involved in several dehydrogenases in the body. The removal of flavin proteins from the metabolic process plays a vital role in the formation of adenosine triphosphate (ATP) via the transfer of hydrogen. Lyases can break down proteins and carbohydrates, thereby providing hydrogen donors for bacterial respiratory processes. Therefore, these data demonstrated that the formation of ATP in bacteria cultured on the Ti-PdH_x surface was suppressed.

Gene set enrichment analysis GSEA (Figure 4e) was performed to further confirm the molecular functions involved in the regulation of bacterial behavior cultured on H_2-loaded Pt films. The normalized enrichment scores (NES) for NADP binding, ATP binding, ATPase activity, and the tricarboxylic acid cycle were −1.926, −1.822, −1.495, and −0.63, respectively. This indicates that ATP-related behavior is negatively regulated. Notably, the ATP-binding cassette (ABC) transporter complex was also downregulated, with an NES value of -1.537. The ABC transporter is an ATPase on the bacterial plasma membrane that can transport ions, amino acids, nucleotides, polysaccharides, peptides, and even proteins. Essential nutrient uptake-related behaviors are highly dependent on ABC transporters. Therefore, the negatively regulated ABC transporter complex implies that the nutrient transport-related behaviors of bacteria cultured on the Ti-PdH_x surface are inhibited. Overall, the data from the transcriptome sequence analysis further confirmed that ROS damage, ATP suppression (which influences the metabolic and biosynthetic processes of amino acids), and nutrient transport inhibition were the main antibacterial mechanisms of the PdH_x film modified Ti (Figure 4f).

2.3. Immune Microenvironment Regulation and Molecular Mechanism Verification

Figure 5a shows the expression of M1- and M2-related genes in the bone marrow-derived macrophages (BMDMs) cultured on various surfaces. In terms of M2-related genes, compared to the Ti group, the Ti-Pd group exhibited higher expression of CD206 and IL-10 genes, especially CD206 ($p < 0.001$). Notably, the Ti-PdH_x group showed significantly higher CD206, Arg, and IL-10 gene expression levels than the Ti group. As for M1-related genes (TNF-α, IL-6, and iNOS), the Ti-Pd and Ti-PdH_x groups

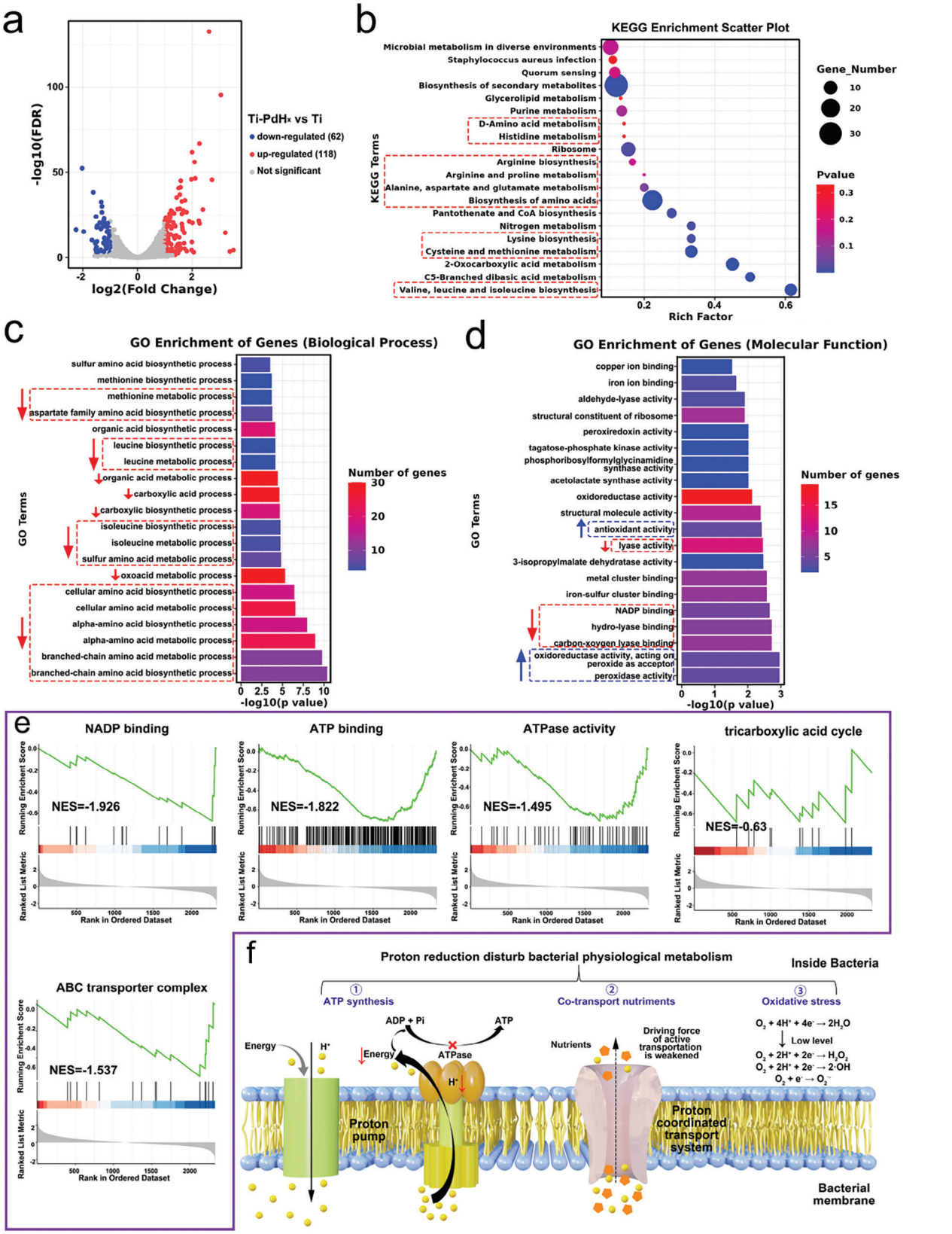

Figure 4. Transcriptome sequence analysis of antibacterial mechanism (Ti–PdH_x vs. Ti). Volcano plot of DEGs (a). The top 20 enriched DEG pathways using the Kyoto Encyclopedia of Genes and Genomes (KEGG) analysis (b). The top 20 enriched biological processes (c) and molecular function using Gene Ontology (GO) analysis (d). Red arrows indicate downregulation, while blue arrows indicate upregulation. Gene set enrichment analysis of the regulated genes with the GO database (e). Schematic illustration of the mechanism of proton transfer-mediated bacterial killing (f).

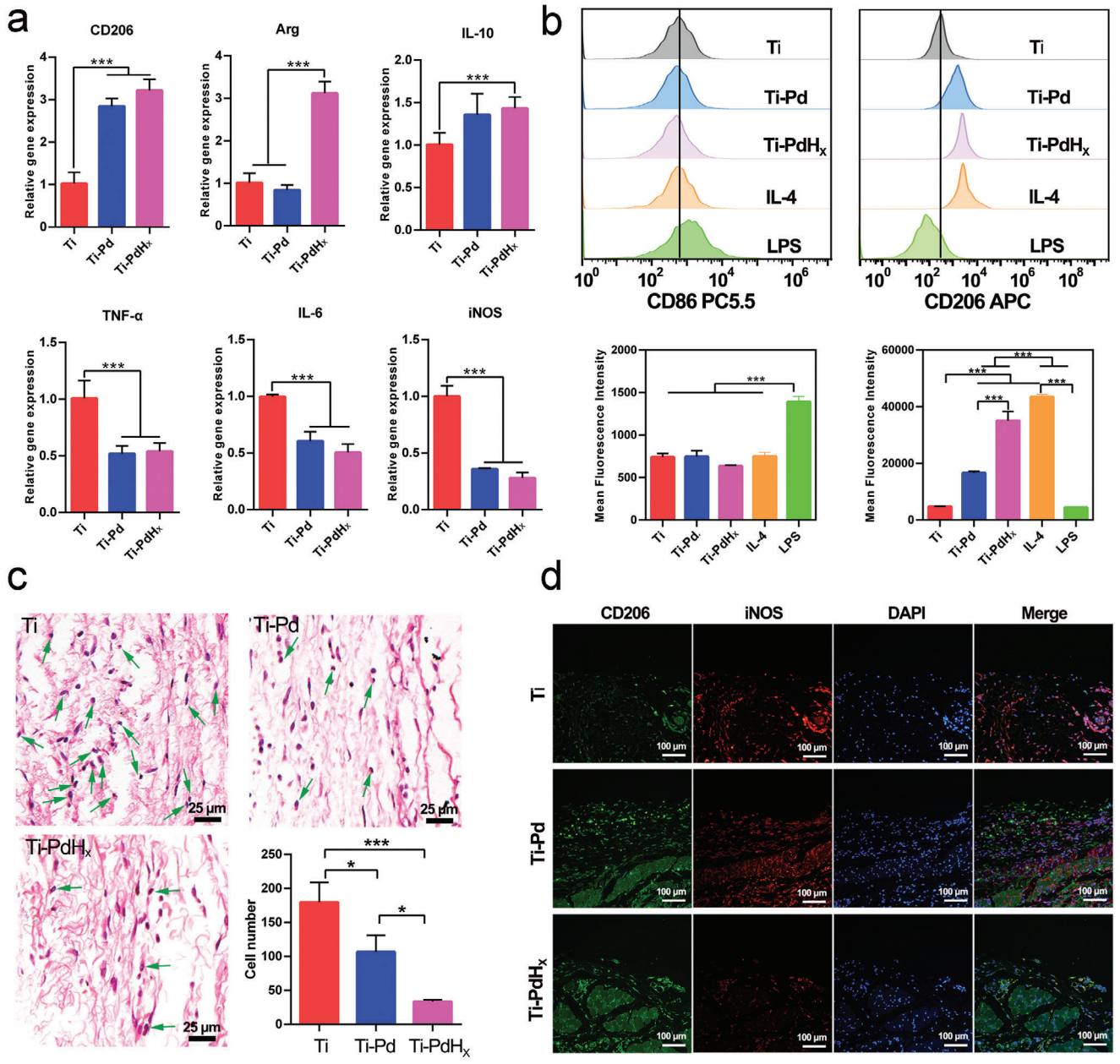

Figure 5. Immune responses of bone marrow-derived macrophages (BMDMs) for various groups. Relative mRNA expression of polarization-related genes in BMDMs after being cultured on various surfaces for 3 days (a). Flow cytometry results of CD86 (M1 marker) and CD206 (M2 marker) in BMDMs after 3 days of culturing on various surfaces (b). Hematoxylin & eosin staining (c), and immunofluorescence staining (d) of the tissue surrounding the implants after being subcutaneously implanted for 4 days.

showed few differences, but both were lower than those of the Ti group. These data indicate that the Pd and H_2-modified Ti surfaces enhance the M2 polarization of BMDMs while inhibiting M1 polarization. Furthermore, the flow cytometry results suggested that the CD206 protein was expressed at high levels in the cells of the Ti-Pd and Ti-PdH$_x$ groups (Figure 5b), which is inconsistent with the reverse-transcription PCR (RT-PCR) results. There was no significant difference in the CD86 protein expression between the groups, in contrast to the RT-PCR results. This may be because flow cytometry mainly analyzes the surface markers of a single cell, which cannot accurately represent the total amount of protein expressed in all cells. A subcutaneous air pouch model was constructed to evaluate the in vivo immune response of the samples. As shown in Figure 5c, the number of inflammatory cells detected exhibited the following trend: Ti > Ti-Pd > Ti-PdH$_x$. Immunofluorescence staining confirmed that the tissue surrounding the Ti-PdH$_x$ implant showed the highest CD206 protein expression and the lowest CD86 protein expression (Figure 5d). These data demonstrate that Ti-PdH$_x$ can reprogram immune cell polarization to a

phenotype that is more favorable to tissue repair, both in vitro and in vivo.

The findings from the CAT, SOD, and DPPH• colorimetric assays reveal that Ti-Pd possesses antioxidative properties (Figure 2d–f), indicating its potential immunomodulatory effects. Moreover, when further hydrogenated, the PdH_x film exhibits enhanced antioxidant enzyme activity, functioning in the initial phase of inflammation and rapidly eliminating oxidizing agents from inflamed tissue. Moreover, the released reduced H_2 can act in the later stages of inflammation at the cellular level to promote the activation of M2-type macrophages, reshape the osteogenic immune microenvironment, and achieve both anti-inflammatory and osteogenesis/angiogenesis-promoting therapeutic effects.[34–36]

The results of both the BMDM culture and air pouch model revealed that the Ti-PdH_x sample could better stimulate the M2 polarization of immune cells than the Ti sample. To further investigate the underlying molecular mechanism of immune regulation in the Ti-PdH_x samples, RNA sequencing was used to evaluate the whole gene expression profiles of BMDMs cultured on the Ti and Ti-PdH_x samples. As shown in **Figure 6a**, Pearson's correlation values (>0.94) demonstrated good clustering between the two analyzed groups. Figure 6b shows a volcano plot, which suggests that more DEGs were downregulated than upregulated when Ti was modified with PdH_x film. Compared to the Ti group, the BMDMs cultured on Ti-PdH_x showed only 131 significantly upregulated and 401 significantly downregulated genes (Figure 6c). These data indicate that the immune regulatory ability of the Ti-PdH_x samples may be correlated with the inhibition of the polarization signaling pathway in BMDMs.

GO and KEGG analyses were used to further investigate the signaling pathways involved. Figure 6d shows the GO enrichment bar plot. DEGs were mainly concentrated in the immune system and innate immune response biological processes. In terms of cellular components, the largest number of DEGs were involved in the membrane and cytoplasm. In terms of molecular function, the DEGs are mainly focused on protein binding. Based on these data, it can be concluded that the H_2-loaded Pd film on Ti can significantly influence proteins on the cell membrane and cytoplasm, rebuilding the immune responses of BMDMs. The top 20 significantly differentially expressed signaling pathways identified by KEGG enrichment analysis are shown in Figure 6e. Four typical signaling pathways participate in immune behavior: the NOD-like receptor, TNF, MAPK, and PI3K-Akt signaling pathways. Among these, the NOD-like receptor signaling pathway, which consists of pattern recognition receptors that generate an innate immune response, is the most differentially expressed signaling pathway.[37] In addition, this signaling pathway functions in the cytoplasm. Therefore, combined with the GO analysis, we believed that the NOD-like receptor signaling pathway is most likely to be involved in regulating the immune behavior of BMDMs cultured on Ti-PdH_x. The KEGG results were analyzed using the NES (ES; Figure 6f–h). NF-κB and MAPK are the downstream signaling pathways of the NOD-like receptor.

The integration of the NOD receptor signaling pathway with downstream MAPK and NF-κB signaling pathways entails complex interactions and signal transductions. Upon ligand recognition, the NOD receptor initiates its signaling cascade, involving receptor conformational changes that recruit and activate downstream signaling molecules. Activated NOD receptors engage adaptor proteins like RIP2 (receptor-interacting protein 2) to form a complex, subsequently activating the downstream MAPK and NF-κB signaling pathways.

In the MAPK pathway, a cascade of kinases is activated sequentially, ultimately leading to the activation of specific transcription factors, such as AP-1, which regulate gene expression. Within the NF-κB signaling pathway, the downstream signaling molecules activated by the NOD receptor prompt the activation of the IKK (IκB kinase) complex, followed by IκB phosphorylation, release of NF-κB from the IκB-NF-κB complex, and NF-κB entry into the nucleus to regulate gene expression. The collective activation of these signaling pathways orchestrates macrophage polarization. Additionally, NLRs initiate a signaling cascade that results in the formation of multiprotein complexes called inflammasomes. These inflammasomes activate caspase-1, which subsequently cleaves and activates proinflammatory cytokines such as IL-1β, IL-6, IL-18, and TNF-α, contributing to macrophage polarization.[38,39]

The ES values of the NOD-like receptor, NF-κB, and MAPK signaling pathways were −0.509, −0.485, and −0.316, respectively, indicating that they were all negatively regulated. Heat maps of the NOD-like receptor-related DEGs are shown in Figure 6i. All 17 DEGs were downregulated in the Ti-PdH_x group compared to the Ti group, suggesting overall downregulation of the NOD-like receptor signaling pathway. In addition, the genes displayed in Figure 6i were further confirmed by RT-PCR, which showed the same trend of downregulated genes as in the Ti-PdH_x group (Figure S8, Supporting Information).

NOD1 and NOD2 are prototypical NOD-like receptors.[40] The western blotting revealed that the two proteins were downregulated in the Ti-PdH_x group (Figure 6j). NOD can activate RIP2 and recruit TAK1. RIP2 and TAK1 expression were also inhibited in the Ti-PdH_x group (Figure 6j). TAK1 is a kinase that is well known to activate the NF-κB and MAPK signaling pathways, which are both pro-inflammatory.[41,42] Considering that the PdH_x film on Ti can reduce ROS via the catalytic ability of Pd and the reduction ability of H_2, the underlying molecular mechanism can be described as follows (Figure 6k): Pd on the Ti surface cooperates with the released H_2 to alleviate the excessively oxidized microenvironment both in extracellular and intracellular terms, and thus negatively regulate NOD1 and NOD2; accordingly, the downstream RIP2 and TAK1 are also inhibited. Finally, NF-κB and MAPK are inactivated, resulting in an anti-inflammatory phenotype in the immune cells. Therefore, the downregulation of NOD-like receptors plays a crucial role in the immune regulation of Ti-PdH_x implants.

2.4. Bone Regeneration and Integration Evaluation In Vitro and In Vivo

Macrophages adapt to local microenvironments and differentiate into either M1 (pro-inflammatory) or M2 (anti-inflammatory) phenotypes, each with distinct functions that influence bone repair.[43,44] M1 macrophages release several pro-inflammatory cytokines (e.g., TNF-α, IL-6, and IL-1β), which can instigate osteoclast activity, cause bone resorption, promote fibrous capsule

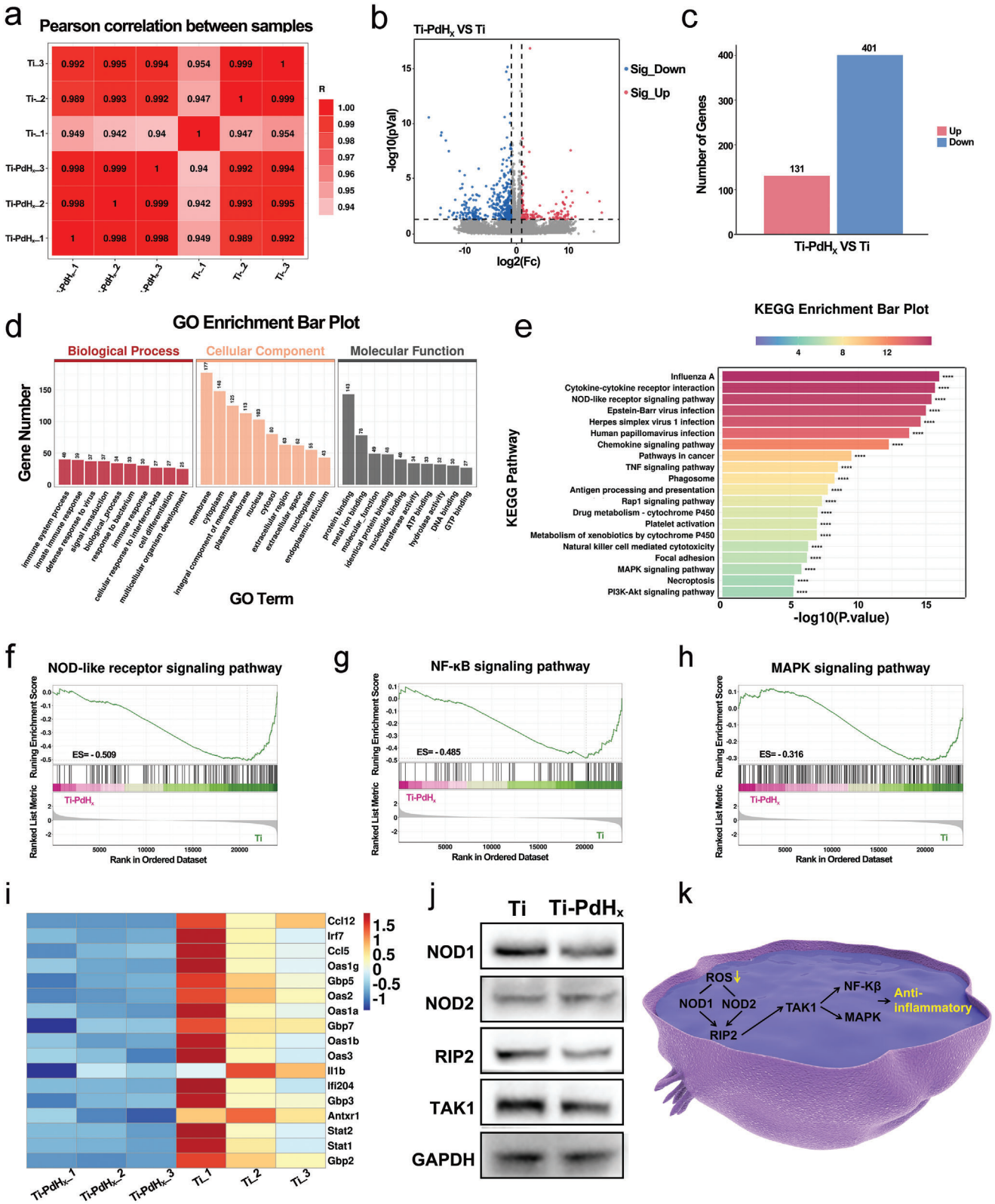

Figure 6. Molecular mechanism study of immune response. Pearson correlation of the groups (a). Volcano plot of differentially expressed genes (DEGs) of Ti-PdH$_x$ vs. Ti (b) and corresponding DEG amounts (c). Analysis of enriched DEGs using Gene Ontology (GO) (d) or Kyoto Encyclopedia of Genes and Genomes (KEGG) (e). Gene set enrichment analysis of the regulated gene pathways with the KEGG and Genomes database (f–h). Heat maps of NOD-like receptor signaling pathway-related DEGs (i). Protein expression in bone marrow-derived macrophages (BMDMs) cultured on Ti and Ti-PdH$_x$ surfaces (j). Schematic illustration of Ti-PdH$_x$ samples regulating immune responses (k).

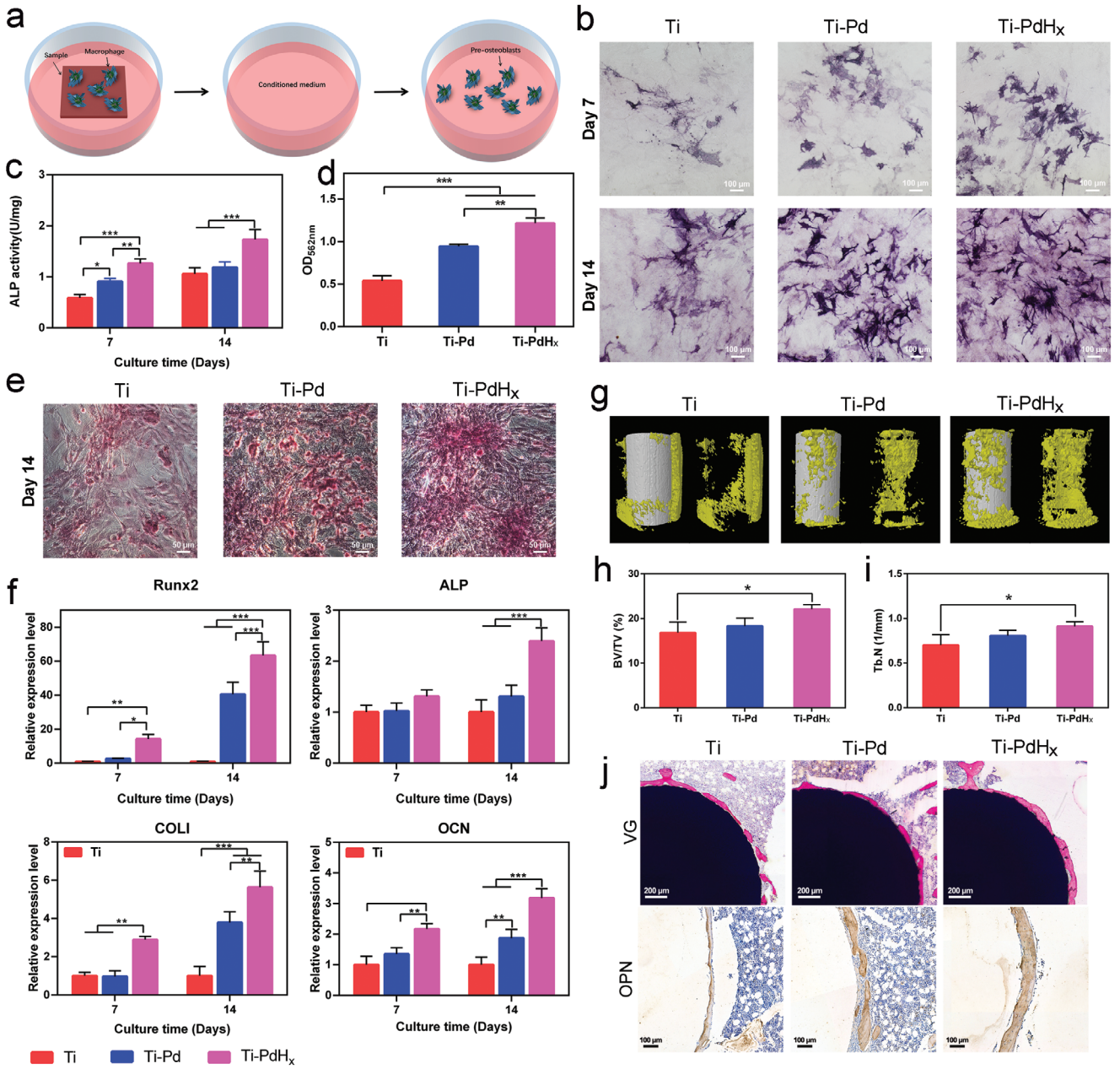

Figure 7. Immunomodulatory osteogenesis evaluation of Ti, Ti-Pd, and Ti-PdH$_x$. In vitro tests: schematic diagram of the culture process of immune-regulated osteoblasts (a); quantitative and qualitative results of ALP activity (b,c) and matrix mineralization activity (d,e); and expression of osteogenesis-related genes, including Runx2, ALP, COL1, and OCN (f). In vivo tests: 3D reconstruction images of micro-computed tomography (CT) results (g); calculated bone volume/tissue volume (BV/TV) values (h) and Tb.N values (i); Van Gieson stain and osteopontin immunostaining (j).

formation, and impede new bone integration. In contrast, M2 macrophages secrete factors (such as IL-10, TGF-β, VEGF, and BMP-2) that foster osteogenesis and angiogenesis, shape the osteoimmune microenvironment, reduce fibrous capsule formation, and promote anti-inflammatory and osteogenic/angiogenic responses.[45,46]

To elicit varying degrees of macrophage polarization and cytokine secretion, macrophages were cultured on the surface of samples and the resulting conditioned medium was used to incubate stem cells (**Figure** 7a). Subsequent analysis of alkaline phosphatase (ALP) activity and extracellular matrix (ECM) mineralization provided both quantitative and qualitative data, as depicted in Figure 7b–e. Representative ALP staining and mineralized nodule images suggested an osteogenic activity trend of Ti-PdH$_x$ > Ti-Pd > Ti. The congruent quantitative data corroborated this observation. After 7 and 14 days of culture, osteogenesis-related gene expressions of Runx2, ALP, COL1, and OCN were measured via RT-PCR, with the highest levels detected in the Ti-PdH$_x$ group at both time points (Figure 7f). Despite no significant difference in ALPL gene expression amongst the groups on day 7,

by day 14, these genes exhibited the most pronounced expression in the Ti-PdH_x group.

An in vivo bone-implantation model investigated the osteointegration of different implants. Newly formed bone reconstruction around the implants was visualized in Figure 7g, while Figure 7h,i displays the bone volume-to-tissue volume (BV/TV) ratio and trabecular number (Tb.N) values. The Ti-PdH_x group demonstrated the highest new bone formation compared to the others, as evidenced by the substantial Van Gieson (VG) staining shown in Figure 7j, indicating pronounced bone growth around Ti-PdH_x samples. Additionally, opulent osteopontin (OPN)-positive regions encircled the Ti-PdH_x implants. Taken together, these findings underscore the superior osteogenic and osteointegrative potential of the Ti-PdH_x implant in vivo.

3. Conclusion

In summary, we fabricated the PdH_x film using ion sputtering and immersion treatment under H_2 gas flow, which showcased multiple biological functions through various biological pathways, thereby improving the clinical significance of this modified implant surface for orthopedic applications. The PdH_x lattice can capture protons in the extracellular microenvironment of bacteria and disrupt their normal physiological metabolic activities, including ATP synthesis, nutrient co-transport, and oxidative stress, leading to bacterial death. Transcriptome sequence analysis of the bacteria revealed an increase in oxidation- and reduction-related activities, while ATP-related and nutrient transport activities were suppressed, suggesting that oxidative damage, energy generation dysfunction, and nutrient deficiency are the primary antibacterial mechanisms of the PdH_x film. Moreover, the PdH_x film can regulate ROS both extracellularly and intracellularly through enzyme catalysis and hydrogen release, thereby reshaping the osteogenic immune microenvironment toward enhanced osteogenesis. Transcriptome sequence analysis of BMDMs indicated that the downregulation of the NOD-like receptor signaling pathway plays a crucial role in activating immune cells to undergo M2 phenotype polarization, thus promoting bone tissue repair.

4. Experimental Section

Sample Preparation: The PdH_x film was prepared by a two-step method. Pd film was fabricated on Ti substrate by using magnetron sputtering (denoted as Ti-Pd), and then H_2 was loaded on Pd film by immersing in Hydrogen gas flow for 6 h at temperature (denoted as Ti-PdH_x).

Surface Characterization: The surface and cross-sectional topographies of samples were characterized by scanning electron microscopy (S-3400N, HITACHI, Japan). The chemical compositions of samples were investigated by energy dispersive spectrometry (IXRF-550i, IXRF SYSTEMS, USA). The crystal phase was measured by X-ray diffraction (D2PHASE, BRUKER, USA). The surface chemical state was investigated by XPS (RBD upgraded PHI-5000C ESCA system, USA). The focus ion beam technique and TEM (FEI Tecnai G2 20 S; EMU) were conducted to investigate the lattice images and crystal structure of the samples.

Water Contact Angle: The water contact angles of the samples were detected by a contact angle measurement (SL200B, Solon, china) by dropping a water droplet with a volume of 2 µL.

Corrosion Resistance: Tafel polarization curves were tested using an electrochemical workstation (CH1760C) at a scan rate of 10 mV s^{-1} from −2 to 0 V.

H_2 Release Measurement: The ability of Ti-PdH_x to release H_2 was demonstrated by using DPPH• (Sigma) as an H_2 probe due to its strong oxidability. In detail, DPPH• was dissolved in anhydrous ethanol at a concentration of 200 µM. Then, 1 mL DPPH• ethanol solution was incubated with Ti-Pd and Ti-PdH_x at 37 °C. After various incubated times (0, 1, 2, 3, 7, 9, 23, and 33 h), 200 µL reactive solution was extracted to measure the absorbance at 517 nm. H_2 release was calculated as the following formula:

$$H_2\text{release}(\%) = \frac{\left(A_{oTi-Pd} - A_{oTi-PdH_x}\right)}{\left(A_p - A_n\right)} \times 100\% \quad (3)$$

where, A_o, A_n, and A_p are the absorbance of the treated samples (Ti-Pd and Ti-PdH_x), negative control (without DPPH•), and positive control (without samples), respectively.

Sod-Like Activity Assays (O_2^- Scavenging Assays): The SOD-like activities of samples were evaluated by total superoxide dismutase assay kit with Tetrazolium salt-2-[2-methoxy-4-nitrophenyl]-3-[4-nitrophenyl]-5-[2,4-disulfophenyl]-2H-tetrazolium (WST-8, Beyotime, Shanghai, China) according to the manufacturer's instructions. Various samples (Ti, Ti-Pd, and Ti-PdH_x) were added to the working solution. The absorbance at 450 nm and UV–vis spectra were measured using a multi-functional microplate reader (Cytation5, BioTec, USA) after standing for 30 min. $O_2^{\bullet-}$ elimination was calculated as the following formula:

$$O_2^{\bullet-}\ \text{elimination}(\%) = \text{Inhibition percentage}(\%) = \frac{\left(B_p - B_o\right)}{\left(B_p - B_n\right)} \times 100\% \quad (4)$$

where, B_o, B_n, and B_p are the absorbance of the treated samples (Ti, Ti-Pd, and Ti-PdH_x), negative control (buffers), and positive control (without samples), respectively.

Cat-Like Activity Assays (H_2O_2 Scavenging Assays): The CAT-like activities of samples were determined by $Ti(SO_4)_2$ chromogenic measurements, which could evaluate the H_2O_2 consumption of samples. Ti, Ti-Pd, and Ti-PdH_x were incubated in 1 mL PBS buffers at 37 °C with 5 mM H_2O_2. After reacted for 12 h, 200 µL of the working solution was mixed with 20 µL of 1% $Ti(SO_4)_2$ for 5 min absolutely. Then the absorbance of the mixture solution at $\lambda = 405$ nm and UV–vis spectra was measured by a multi-functional microplate reader. H_2O_2 elimination was calculated as the following formula:

$$H_2O_2\ \text{elimination}\ (\%) = \frac{\left(C_p - C_o\right)}{\left(C_p - C_n\right)} \times 100\% \quad (5)$$

where, C_o, C_n, and C_p are the absorbance of the treated samples (Ti, Ti-Pd, and Ti-PdH_x), negative control (without $Ti(SO_4)_2$), and positive control (without samples), respectively.

DPPH Scavenging Assays: DPPH• as a typical RNS was used to study the samples' RNS scavenging activity. DPPH• (200 µM) dissolved in ethanol was co-cultured with samples at 37 °C for 6 h. The absorbance at 517 nm and the absorption spectra were measured by a multi-functional microplate reader. DPPH• elimination was calculated as the following formula:

$$\text{DPPH elimination}(\%) = \frac{\left(D_p - D_o\right)}{\left(D_p - D_n\right)} \times 100\% \quad (6)$$

where, D_o, D_n, and D_p are the absorbance of the treated samples (Ti, Ti-Pd, and Ti-PdH_x), negative control (without DPPH•), and positive control (without samples), respectively.

Bacterial Culture and Cell Activity Tests: Gram-positive *S. aureus* was used to evaluate the antibacterial activities of the various samples. *S. aureus* solution (50 µL) with a concentration of 10^7 CFU mL^{-1} was seeded in the surface of Ti, Ti-Pd, and Ti-PdHx for 24 h. Afterward, all samples were transferred into tubes with 4 mL of 0.9 wt.% NaCl solution and dissociated bacteria. Subsequently, the solutions were diluted 10 times and spread onto a standard agar culture plate. After 18 h, the bacterial colonies were obtained and counted. Image J software was used to count the colonies. The activity of the cells was measured by AlamarBlue assay.

Live/Dead Staining Assay of Bacteria: *S. aureus* (1×10^7 CFU) was cultured on various samples for 24 h and then washed with PBS for three times. After that, the bacteria adhered on the sample surfaces were stained using BBcellProbe N01/PI (Biosen, Shanghai). Afterward, the stained samples were washed using PBS and the live (green fluorescence)/dead (red fluorescence) bacteria were observed under a fluorescence microscope.

CTC Staining of Bacteria: 5-cyano-2,3-ditolyl Tetrazolium Chloride (CTC) staining was employed to observe changes in the mitochondrial membrane potential of *S. aureus* after treating Ti, Ti-Pd, and Ti-PdH_x ($n = 3$). After incubated at 37 °C for 12 h, 1 mL of normal salt was added to rinse samples twice. Then, CTC staining working solution (500 µL) was put into the bacteria and incubated at 37 °C for 30 min. Subsequently, the supernatant was removed and the sample with bacteria was washed using a CTC staining buffer. Fluorescence images were recorded by fluorescence microscope.

ATP Level Detection: The Enhanced ATP Assay Kit (Beyotime, China) was used to evaluate the level of ATP expression in bacteria. *S. aureus* liquid (50 µL; $OD_{600nm} = 0.2$) was seeded in the surface of Ti, Ti-Pd, and Ti-PdH_x ($n = 3$). After incubated at 37 °C for 10 h, the sample was transferred to a centrifuge tube containing 1 mL physiological saline and continue vortexed for 30 s to collect bacteria. Extractions of the ATP production in bacterial cells were done complying with the kit instruction, the fluorescence intensity was measured by a luminometer on the multi-functional microplate reader. The ATP concentration of the samples was obtained according to the standard curve.

In Vitro ROS Detection: *S. aureus* (1×10^7 CFU) was cultured on various samples for 6 h. After washed with PBS, the bacteria on the sample surfaces were stained with BBoxiProbe O12 solution (BBestbio) for 30 min. The stained bacteria were washed using PBS and observed under the fluorescence microscope.

RNA Sequence Analysis of S. aureus: *S. aureus* (1×10^7 CFU) was cultured on various samples for 6 h. Then *S. aureus* was collected to extract the total RNA using TRIzol reagent (Invitrogen, CA, USA). RNA sequencing was performed via the HiSeq 4000 SBS Kit (300 cycles; Illumina, CA, USA). Data analysis was performed by FastqStat.jar (v0.11.4) and RSeQC (v2.6.4). Gene Ontology (http://www.geneontology.org) and Kyoto Encyclopedia of Genes and Genome (http://www.genome.jp/kegg/) were used to analyze the gene functions.

In Vivo Antibacterial Evaluation: All the animals used in this study were purchased from the Medical Experimental Animal Center of Guangdong Province and the experiments were authorized by the Animal Ethics Committee of Guangdong Provincial People's Hospital (KY-Q-2021-236-0). In prior of the surgery, the implants (Φ 2 × 4 mm) were immersed in 600 µL of *S. aureus* (1×10^6 CFU mL^{-1}) for 15 min and then rinsed twice with PBS. Eighteen Sprague–Dawley rats (male, 8 weeks old) were anesthetized. The femoral condyles of both sides were exposed, and then holes with a diameter of 2 mm were drilled vertically to the femoral shaft. Each hole was implanted with one specimen. After 1 and 4 days of the surgery, the implants were collected and rolled over the agar plates. In addition, the femoral condyles were fixed, decalcified, dehydrated, embedded, sliced, and finally stained with H&E and Giemsa.

Real-Time Polymerase Chain Reaction (RT-PCR): BMDMs were isolated from the femurs and tibia of C57BL mice. The culture medium was 1640 medium (RPMI-1640; Gibco, USA) supplemented with FBS (10%) and granulocyte-macrophage colony-stimulating factor (Peprotech, USA).

After BMDMs (5×10^4) were seeded onto various samples for 3 days, RNA in the cells was extracted using E.Z.N.A. Total RNA Kit (Omega Bio-Tek, USA), and then reversely transcribed into cDNA using TransScript First-Strand cDNA Synthesis SuperMix Kit (TransGen, Biotech, China). The cDNA was analyzed on the Bio-Rad CFX 96 RealTime System using a mixture of SYBR Green Realtime PCR Master Mix (Transgen Biotech, China). The expression of M1-related genes, including nitric oxide synthase (iNOS) and tumor necrosis factor α (TNF-α) and interleukin 6 (IL-6), and M2-related genes, including CD206, interleukin 10 (IL-10) and auxin-regulated gene (Arg), were evaluated, and the corresponding sequences are shown in Table S1 (Supporting Information). The house-keeping gene was glyceraldehyde-3-phosphate dehydrogenase (GAPDH).

Flow cytometry Analysis: BMDMs (5×10^4) were seeded onto various samples. The cells cultured on Ti were simulated with Interleukin 4 (IL-4) and Lipopolysaccharide (LPS) to work as M2-polarization and M1-polarization control, respectively. After cultured for 3 days, the cells were gently collected. The collected cells were centrifuged and resuspended in Dulbecco's PBS (DPBS) and then incubated with fluorescently labeled primary monoclonal antibodies, including macrophage phenotype markers (PC5.5 mouse anti-F4/80, FITC mouse anti-CD11B; BD Biosciences, USA) and M1 phenotype marker (PC7 mouse anti-CD86; BD Biosciences, USA). After incubated for 15 min, the cells were washed with staining buffer and then centrifuged. The cells were then fixed and permeabilized in a fixation/permeabilization solution, and stained with M2 phenotype marker (APC mouse anti-CD206; BD Biosciences, USA) for 30 min. Finally, the cells were washed with Perm/Wash buffer and resuspended in a staining buffer for flow cytometry using a Beckman flow cytometer (CytoFLEX, USA). The results were analyzed using FlowJo software.

In Vivo Mouse Air-Pouch Model: Nine Balb/c mice (male, 6 weeks old) were anesthetized and the hair in the back was shaved. Then, 3 mL of sterilized air was injected subcutaneously into the back of the mice and 2 mL of sterilized air was injected 4 days later to form stable air pouches. After another 3 days, the samples were implanted into the pouches. The tissues covering the implants were collected after 4 days of implantation. The collected tissues were fixed, embedded, sliced, and finally stained with hematoxylin-eosin (H&E). In addition, the sliced tissues were also subjected to immunofluorescence staining with CD206 (1 µg mL^{-1}) and iNOS (1 µg mL^{-1}).

RNA Sequence Analysis of BMDMsdms: BMDMs (1×10^5) were cultured on Ti and Ti-PdH_x for 3 days. The total RNA was isolated using TRIzol reagent (Invitrogen, USA) and its integrity was assessed using Bioanalyzer 2100 (Agilent, CA, USA). The RNA was then purified, fragmented into small pieces, and reverse-transcribed to cDNA. The cDNA was then reacted with *E. coli* DNA polymerase I (NEB, cat.m0209, USA), RNase H (NEB, cat.m0297, USA) and dUTP Solution (Thermo Fisher, cat. R0133, USA) to form U-labeled second-stranded DNAs. The blunt ends of each strand were added with an A-base and then the fragment size was screened and purified using magnetic beads. Thereafter, the U-labeled second-stranded DNAs were treatment with UDG enzyme (NEB, cat.m0280, USA) and then amplified with PCR. The qualified samples were performed the 2 × 150 bp paired-end sequencing (PE150) on an Illumina Novaseq 6000 (LC-Bio Technology CO., Ltd., China) following the vendor's protocol. The differentially expressed mRNAs were selected with fold change > 2 or fold change < 0.5, and *p*-value < 0.05. Bioinformatic analysis was performed using the OmicStudio tools at https://www.omicstudio.cn/tool.

Preparation of Macrophage-Conditioned Medium (MCM): BMDMs (5×10^4) were seeded onto various samples for 3 days, and then the supernatant was collected and centrifuged to remove the suspended cells. The collected supernatant was added with 10% FBS and osteogenic induction solution (10 mM β-glycerophosphate, 100 nM dexamethasone, 50 mM ascorbate, and glutamine), and denoted as MCM for the following experiments.

Alkaline Phosphatase (ALP) Activity: MC3T3-E1 (3×10^4) were cultured in the above MCM for 7 and 14 days. Thereafter, the BCIP/NBT ALP Color Development Kit (Beyotime Biotechnology, China) was used to stain the ALP in the cells and then observed using an optical microscope (Olympus, Japan). Meanwhile, intracellular ALP activity was quantitatively evaluated using the ALP Assay Kit (Beyotime Biotechnology, China), and the results were normalized to the total intracellular protein content using the BCA Protein Assay Kit (Thermofisher Scientific, USA).

Extracellular Matrix (ECM) Mineralization: MC3T3-E1 (3×10^4) were cultured in the above MCM for 14 days. Thereafter, the cells stained with

alizarin red (AR; 40 mM, Leagene Biotechnology) and observed using an optical microscope. The bonded dye was quantitatively analyzed by dissolving in 10% cetylpyridinium chloride (Sigma-Aldrich, USA), and the absorbance of the solution at 620 nm was measured.

Bone-Related Genes Expression: MC3T3-E1 (3×10^4) were cultured in the above MCM for 7 and 14 days. Thereafter, RNA in the cells was extracted and then reversely transcribed into cDNA as mentioned before. The expression of genes, including Runx2, ALP, COLI, and OCN were evaluated, and the corresponding sequences are shown in Table S1. The house-keeping gene was glyceraldehyde-3-phosphate dehydrogenase (GAPDH).

In Vivo Bone Regeneration Evaluation: The implants without bacteria contamination were implanted into the femoral condyles ($n = 6$ for each group) for 8 weeks. The femoral condyles were then scanned using a Micro-CT analyzer (Inveon Multi-Modality; Siemens Medical Solutions, Germany). The bone volume percentage (BV/TV) and trabecular number (Tb.N) values were calculated using VG Studio MAX software, while the 3D images were reconstructed using Multimodal 3D Visualization (Siemens Medical Solutions, German) software. Thereafter, the femoral condyles were fixed, embedded, sliced, and finally stained with Van Gieson's (VG) solution and observed under an optical microscope. Meanwhile, some of the collected femoral condyles were decalcified, dehydrated, embedded, sliced, and finally stained with OPN.

Supporting Information

Supporting Information is available from the Wiley Online Library or from the author.

Acknowledgements

D.Z., M.L., and S.C. contributed equally to this work. This work was financially supported by the Key Research and Development Program of Zhejiang Province (Grant No. 2023C03G9103957), Shenzhen Science and Technology Funding (Grant No. JCYJ20230807113016033), Natural Science Foundation of Guangdong Province, China (Grant No. 2023A1515110092), National Natural Science Foundation of China (Grant No. 52371252 and 82372375), General Research Fund of the Research Grants Council (17214516,17207719,1711322), Hong Kong Health and Medical Research Fund (20190244,21200592), Collaborative Research Fund of the Hong Kong Research Grants Council (C5044-21G).

Conflict of Interest

The authors declare no conflict of interest.

Data Availability Statement

The data that support the findings of this study are available from the corresponding author upon reasonable request.

Keywords

bacterial killing, enzyme-like activity, osteogenic immune microenvironment, palladium hydride film, Proton transfer

Received: March 27, 2024
Revised: May 13, 2024
Published online: May 27, 2024

[1] Q. Chen, G. Thouas, *Mater. Sci. Eng., R* **2015**, *87*, 1.
[2] P. Habibovic, J. Barralet, *Acta Biomater.* **2011**, *7*, 3013.
[3] D. Wang, J. Tan, H. Zhu, Y. Mei, X. Liu, *Adv. Sci.* **2021**, *8*, 2004393.
[4] W. Wang, W. Yeung, *Bioact Mater* **2017**, *2*, 224.
[5] C. Kenney, S. Dick, J. Lea, J. Liu, N. Ebraheim, *J Orthop* **2019**, *16*, 393.
[6] S. Magill, J. Edwards, W. Bamberg, *N. Engl. J. Med.* **2014**, *370*, 1198.
[7] C. Arciola, D. Campoccia, L. Montanaro, *Nat. Rev. Microbiol.* **2017**, *16*, 397.
[8] W. Li, E. Thian, M. Wang, Z. Wang, L. Ren, *Adv. Sci.* **2021**, *8*, 2100368.
[9] Z. Chen, R. Murray, R. Crawford, J. Chang, C. Wu, Y. Xiao, *Mat. Today* **2016**, *19*, 304.
[10] J. Lee, H. Byun, S. Perikamana, S. Lee, H. Shin, *Adv. Healthcare Mater.* **2019**, *8*, 1801106.
[11] C. Hu, D. Ashok, D. Nisbet, V. Gautam, *Biomaterials* **2019**, *219*, 119366.
[12] K. Su, L. Tan, X. Liu, Z. Cui, Y. Zheng, B. Li, Y. Han, Z. Li, S. Zhu, Y. Liang, X. Feng, X. Wang, S. Wu, *ACS Nano* **2020**, *14*, 2077.
[13] J. Fu, Y. Li, Y. Zhang, Y. Liang, Y. Zheng, Z. Li, S. Zhu, C. Li, Z. Cui, S. Wu, *Adv. Mater.* **2021**, *33*, 2102926.
[14] E. Zhao, A. Gao, Q. Liao, Y. Li, I. Ullah, Y. Zhao, X. Ren, L. Tong, X. Li, Y. Zheng, P. Chu, H. Wang, *Adv. Funct. Mater.* **2024**, *34*, 2311812.
[15] C. Zhang, G. Chu, Z. Ruan, N. Tang, C. Song, Q. Li, W. Zhou, J. Jin, H. Haick, Y. Chen, D. Cui, *ACS Nano* **2022**, *16*, 16584.
[16] G. Chu, M. Guan, J. Jin, Y. Luo, Z. Luo, T. Shi, T. Liu, C. Zhang, Y. Wang, *Adv. Mater.* **2024**, *36*, 231185.
[17] L. Shi, H. Dong, G. Reguera, H. Beyenal, A. Lu, J. Liu, H. Yu, J. Fredrichson, *Nat. Rev. Microbiol.* **2016**, *14*, 651.
[18] G. Reguera, K. Mccarthy, T. Mehta, J. Nicoll, M. Tuominen, D. Lovley, *Nature* **2005**, *435*, 1098.
[19] K. Birsoy, T. Wang, W. Chen, E. Freinkman, M. Abu-Remaileh, D. Sabatini, *Cell* **2015**, *162*, 540.
[20] P. Boyer, *Ann. Rev. Biochem.* **1997**, *66*, 717.
[21] C. Ballmoos, *J. Bioenerg. Biomembr.* **2007**, *39*, 441.
[22] Y. Bae, H. Oh, S. Rhee, Y. Yoo, *Mol. Cells* **2011**, *32*, 491.
[23] M. Xu, Y. Zhou, C. Ren, X. Liang, N. Li, *Adv. Funct. Mater.* **2021**, *31*, 202104892.
[24] T. Wang, X. Zhu, F. Wu, *Bioact Mater* **2023**, *23*, 129.
[25] Q. Xu, S. Chen, L. Jiang, C. Xia, L. Zeng, X. Cai, Z. Jin, S. Qin, W. Ding, Q. He, *Natl Sci Rev* **2023**, *10*, nwad063.
[26] Y. You, Y. Zhu, J. Jiang, M. Wang, Z. Chen, C. Wu, J. Wang, W. Qiu, D. Xu, H. Lin, J. Shi, *J. Am. Chem. Soc.* **2022**, *144*, 14195.
[27] I. Ohsawa, M. Ishikawa, K. Takahashi, M. Watanabe, K. Nishimaki, K. Yamagata, K. Katsura, Y. Katayama, S. Asoh, S. Ohta, *Nat. Med.* **2007**, *13*, 688.
[28] Z. Chen, R. Murray, R. Crawford, J. Chang, C. Wu, Y. Xiao, *Mater. Today* **2016**, *19*, 304.
[29] Z. Tu, Y. Zhong, H. Hu, D. Shao, R. Haag, M. Schirner, J. Lee, B. Sullenger, K. Leong, *Nat. Rev. Mater.* **2022**, *7*, 557.
[30] L. Zhang, P. Zhao, C. Yue, Z. Jin, Q. Liu, X. Du, Q. He, *Biomaterials* **2019**, *197*, 393.
[31] R. Bardhan, L. Hedges, C. Pint, A. Javey, S. Whitelam, J. Urban, *Nat. Mater.* **2013**, *12*, 905.
[32] Q. Zhao, L. Zheng, Y. Gao, J. Li, J. Wei, M. Zhang, J. Sun, J. Ouyang, N. Na, *J. Am. Chem. Soc.* **2023**, *145*, 12586.
[33] H. Li, S. Zhang, S. Huo, H. Tang, B. Nie, X. Qu, B. Yue, *J. Orthop. Transl.* **2020**, *21*, 66.
[34] Y. Liu, Y. Cheng, H. Zhang, M. Zhou, Y. Yu, S. Lin, B. Jiang, X. Zhao, L. Miao, C. Wei, Q. Liu, Y. Lin, Y. Du, C. Butch, H. Wei, *Sci. Adv.* **2020**, *6*, abb2695.
[35] Q. Wang, C. Cheng, S. Zhao, Q. Liu, Y. Zhang, W. Liu, X. Zhao, H. Zhang, J. Pu, S. Zhang, H. Zhang, Y. Du, H. Wei, *Angew. Chem., Int. Ed.* **2022**, *61*, 202201101.
[36] M. Li, X. Chu, D. Wang, L. Jian, L. Liu, M. Yao, D. Zhang, Y. Zheng, X. Liu, Y. Zhang, F. Peng, *Biomaterials* **2022**, *282*, 121408.
[37] O. Takeuchi, S. Akira, *Cell* **2010**, *140*, 805.

[38] Y. Guo, H. Zhang, Z. Lv, Y. Du, D. Li, H. Fang, J. You, L. Yu, R. Li, *Cell Commun. Signaling* **2023**, *21*, 66.
[39] S. Huo, S. Liu, Q. Liu, E. Xie, L. Miao, X. Meng, Z. Xu, C. Zhou, X. Liu, G. Xu, *Adv. Sci.* **2024**, *11*, 2302674.
[40] R. Caruso, N. Warner, N. Inohara, G. Nunez, *Immunity* **2014**, *41*, 898.
[41] H. Yun, H. Lee, *Life Sci.* **2023**, *319*, 121388.
[42] J. Totzke, S. Scarneo, K. Yang, T. Haystead, *Open Biol* **2020**, *10*, 200099.
[43] S. Jin, D. He, D. Luo, Y. Wang, M. Yu, B. Guan, Y. Fu, Z. Li, T. Zhang, Y. Zhou, C. Wang, Y. Liu, *ACS Nano* **2019**, *13*, 6581.
[44] L. Tan, J. Fu, F. Peng, X. Liu, Z. Cui, B. Li, Y. Han, Y. Zheng, K. Yeung, Z. Li, S. Zhu, Y. Liang, X. Feng, X. Wang, S. Wu, *Sci. Adv.* **2020**, *6*, aba5723.
[45] L. Chen, D. Wang, F. Peng, J. Qiu, L. Ouyang, Y. Qiao, X. Liu, *Nano Lett.* **2019**, *19*, 3480.
[46] Y. Zhu, H. Liang, X. Liu, J. Wu, C. Yang, T. Wong, K. Kwan, K. Cheung, S. Wu, K. Yeung, *Sci. Adv.* **2021**, *7*, abf6654.